High circular polarization ratios in radar scattering from geologic targets

Bruce A. Campbell[1]

Received 9 February 2012; revised 15 May 2012; accepted 15 May 2012; published 30 June 2012.

[1] We examine and model the occurrence of circular polarization ratio (CPR or μ_c) values greater than unity in terrestrial and planetary radar observations as a guide to the range of associated surface morphology. Lunar crater deposits exhibit maximum μ_c values at 12.6 and 70-cm wavelength of 2 to 3. CPR values for Maxwell Montes on Venus range up to about 1.5 at 12.6-cm wavelength. Echoes from SP Flow in Arizona exhibit μ_c up to 2 at 24-cm wavelength. Scattering from rock edges and cracks (dipole-like) produces μ_c of unity for single scattering and up to about 2 for multiple reflections. Scattering from natural corner reflectors (dihedrals) formed by pairs of rock facets can yield an average μ_c of 3–4, but likely requires non-random or scale-limited surface roughness properties in order to dominate the observed echo. The dihedral mechanism is required to satisfy the highest lunar μ_c observations, while echoes from SP Flow and Maxwell Montes could be explained by just the dipole mechanism. The dihedral scenario requires rocky facets on scales many times the radar wavelength, which the blocks at SP Flow (and the unknown surface texture of Maxwell) may not provide. The random dipole model is less demanding in terms of structures and scales, and likely increases the CPR of lunar or asteroid regoliths through scattering from and between rocks.

Citation: Campbell, B. A. (2012), High circular polarization ratios in radar scattering from geologic targets, *J. Geophys. Res.*, *117*, E06008, doi:10.1029/2012JE004061.

1. Introduction

[2] Radar observations of planetary surfaces have long been used to infer physical properties such as topographic roughness, rock abundance, reflectivity, and dielectric loss. A major advantage in such applications is information on the polarization of the reflected signal. Current airborne and Earth-orbiting radar sensors often measure the complete scattering matrix for each image pixel in "quad-pol" format [*van Zyl et al.*, 1987], which permits analysis of the surface scattering behavior in all possible configurations of the transmitted and received signal polarization. A number of decomposition models have been proposed that use this polarimetric information to estimate the contributions of various surface scattering mechanisms to the observed echo [e.g., *van Zyl*, 1989; *Campbell et al.*, 1989; *Freeman and Durden*, 1998].

[3] For planetary work, a dual-polarization or hybrid-polarization format is used for most Earth-based observations [e.g., *Campbell et al.*, 2007] and for two recent lunar-orbiting radars [*Raney*, 2007]. These radar systems transmit a single polarization and measure reflections in two orthogonal polarization components. The "dual-pol" format allows for a Stokes-vector representation of the echo, and application of techniques that can indicate the degree of subsurface scattering [e.g., *Carter et al.*, 2004, 2011]. The more limited polarimetric information contained in the dual-pol format poses a challenge to understanding surface physical properties from radar remote sensing.

[4] The circular polarization ratio (μ_c or CPR) is measured in both the quad-pol and the typical planetary dual-pol observing format. The CPR, defined as the ratio between power reflected in the same sense of circular polarization (SC) as that transmitted and the echo in the opposite sense (OC) of circular polarization, is strongly modulated by roughness-induced changes in scattering on or beneath a target surface. We have observations of μ_c in a wide range of terrestrial [*Campbell et al.*, 1993; *Rignot*, 1995; *Plaut et al.*, 2004; *Campbell*, 2009] and planetary settings: Mars [*Harmon et al.*, 1999; *Harmon and Nolan*, 2007], the Galilean satellites [*Campbell et al.*, 1978; *Ostro et al.*, 1992], Venus [*Campbell et al.*, 1999; *Carter et al.*, 2004], Mercury [*Harmon et al.*, 1994, 2001, 2011], Titan [*Black et al.*, 2011], asteroids [*Shepard et al.*, 2008; *Benner et al.*, 2008], and the Moon [*Campbell et al.*, 2006, 2009; *Spudis et al.*, 2010].

[5] From these analyses, it is evident that there is considerable information to be gained from the CPR about the physical properties of the surface. For "typical" rough surfaces, such as the suite of textures found in Hawaiian lava flows, μ_c exhibits an increase with incidence angle and topographic roughness on horizontal scales comparable to

[1]Center for Earth and Planetary Studies, Smithsonian Institution, Washington, DC, USA.

Corresponding author: B. A. Campbell, Center for Earth and Planetary Studies, Smithsonian Institution, MRC 315, PO Box 37012, Washington, DC 20013-7012, USA. (campbellb@si.edu)

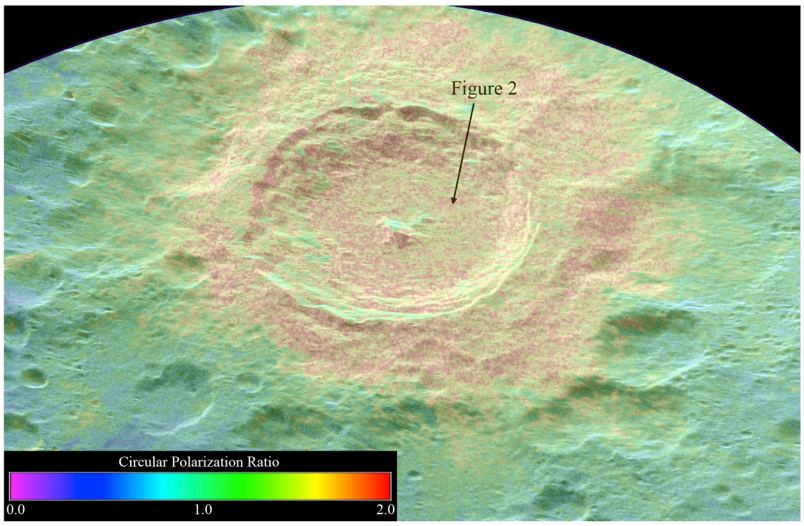

Figure 1. Earth-based 12.6-cm wavelength radar image of the 86-km lunar crater Tycho, with circular polarization ratio as a color overlay. North is toward top; simple cylindrical map projection. Radar incidence angle at the center of the crater is about 42°. Radar look direction is approximately from the upper right [*Campbell et al.*, 2010]. Approximate location of the LROC image in Figure 2 is shown by the arrow.

the observing wavelength, and a maximum value of about 0.6 [*Campbell*, 2009]. In other geologic settings, however, much higher values of the CPR have been observed, raising questions about the scattering mechanism and associated physical properties of the surface or subsurface. For any rocky planetary body, understanding the plausible scattering geometries is directly relevant to understanding the processes that form and modify the surface or regolith. The question here is how various geologic attributes (rock or plate sizes, shapes, proximity, volume distribution in a soil, etc.) may contribute to a strong CPR enhancement.

[6] Water ice that occurs in sheets or slabs at least a few radar wavelengths in thickness has very strong radar backscatter and enhanced circular polarization ratio values. This behavior arises due to scattering by cracks and voids in the ice, which has an intrinsically low microwave loss. Radar signals propagating along a given scattering path through the medium in opposite directions emerge to constructively enhance the same sense of circular polarization as that transmitted [e.g., *Black et al.*, 2001]. As a result, the CPR can have a maximum value of about 2. Values of 1.5 to 1.8 are observed for the Galilean satellites [*Campbell et al.*, 1978; *Ostro et al.*, 1992; *Black et al.*, 2001] and the Greenland ice sheet [*Rignot*, 1995]. A high CPR signature, strong overall backscatter, and the high degree of correlation between radar-bright features and regions of permanent shadow, are the primary arguments for associating echo properties from polar craters on Mercury with sheets of ice [*Harmon et al.*, 1994, 2001, 2011]. An area of strong future interest is radar detection of shallow ice bodies on Mars, which have been observed at the Phoenix landing site [*Smith et al.*, 2009] and in several recent craters in the plains [*Byrne et al.*, 2009]. It is thus important to understand the scattering properties of rocky surfaces and regoliths in order to better discriminate ice deposits using radar echo amplitude and polarization data [e.g., *Fa et al.*, 2011; *Thompson et al.*, 2011].

[7] This paper examines several rough-surface scattering mechanisms that offer reasonable explanations for high CPR values, and compares their predicted polarimetric behavior with examples from lunar and terrestrial settings. Section 2 presents 12.6-cm and 70-cm Earth-based radar observations that illustrate the upper range of circular polarization ratios from rugged lunar impact crater interiors and ejecta. Section 3 uses a Stokes-matrix approach to illustrate how various polarization properties can lead to elevated μ_c values, and notes upper limits to the CPR under different scattering regimes. Section 4 examines radar data for SP Flow, a blocky volcanic deposit in northern Arizona, and shows that high-μ_c pixels are better explained by multiple scattering from random rock edges or cracks than by a dihedral scattering model. Section 5 discusses the significance of these results to the interpretation of current data and the design of future radar investigations.

2. High CPR Values in Lunar Radar Observations

[8] High values of the circular polarization ratio have been noted for both 12.6-cm and 70-cm radar observations of the Moon [e.g., *Campbell et al.*, 2009, 2010; *Spudis et al.*, 2010]. The extreme degree of localized enhancement in μ_c was recognized only recently due to much finer image spatial resolution (10s of meters to a few hundred meters), which can identify patches of very rough or otherwise anomalous terrain. The highest values of μ_c are found in the walls, floors, and proximal ejecta blankets of impact craters. The crater walls and floors are rough due to the presence of rocky debris or lava-like impact melt sheets, while the proximal ejecta is comprised of abundant surface boulders, rocks suspended within the fine-grained regolith, and patches of rough impact melt.

[9] The 86-km crater Tycho is one of the youngest large craters on the Moon, with an age of about 100 m.y. [e.g., *Hiesinger et al.*, 2010], and exhibits high values of backscatter strength and circular polarization ratio (Figure 1). High-resolution (50 cm per pixel) images from the Lunar

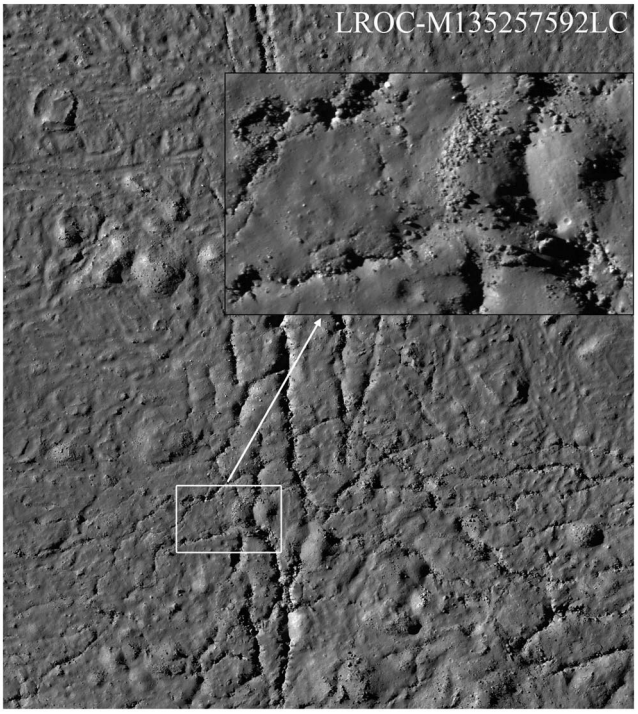

Figure 2. Lunar Reconnaissance Orbiter Camera narrow-angle image of the floor of Tycho crater. Background image is averaged to 2-m spatial resolution; inset shows 50-cm resolution detail of crater floor fissures and surface debris. Solar incidence angle 67°, with illumination from the left. Portion of image M135257592LC.

Reconnaissance Orbiter Camera (LROC) [*Robinson et al.*, 2010] show a complex array of lobes, hills, fissures, and cracks in the crater floor, with a thin regolith cover and abundant boulders (Figure 2). The largest boulders in this image are 10 m or more in diameter, and most of those visible on the surface are 3–6 m in scale. There are patches of smooth-appearing mantling material between the boulder-rich outcrops, but small bright spots and shadows suggest that rocky debris is also present within or just under this cover. The mean 12.6-cm circular polarization ratio of the terrain represented by this LROC image is 1.75.

[10] Figure 3 shows a histogram of μ_c values for 12.6-cm [*Campbell et al.*, 2010] and 70-cm [*Campbell et al.*, 2007] wavelength over the entire crater and out to about one crater radius in the Tycho ejecta blanket (Figure 1). These values are calculated from SC and OC echo data averaged to 100 or more independent looks. The speckle-related uncertainty declines as the root of the number of looks, so the uncertainty in any single power measurement, and by extension the CPR, is about 10% (e.g., $\mu_c = 2.5 \pm 0.25$) or less. As observed for the example site above, the rugged Tycho deposits produce large CPR enhancements. In the 12.6-cm data, maximum values of 2.5 to 3 occur, while the 70-cm echoes reach maximum values of 2 to 2.5.

[11] Values of μ_c up to about 2, at 70-cm and 12.6-cm wavelength, also occur for domes in the Marius Hills, and within/around numerous smaller to moderate-diameter craters [*Campbell et al.*, 2006, 2009; *Spudis et al.*, 2010]. As an

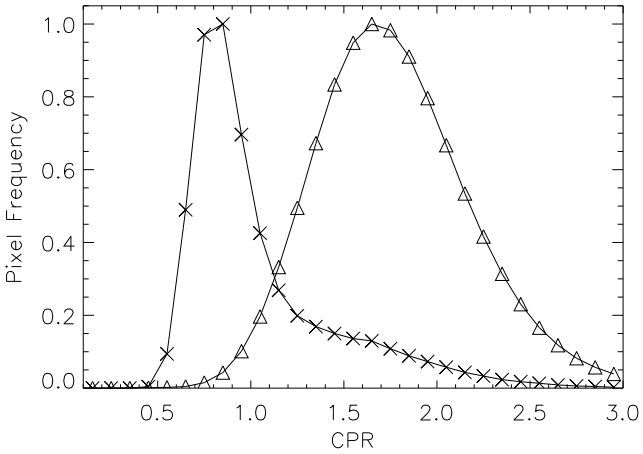

Figure 3. Histograms of CPR values for the Tycho crater floor and proximal ejecta blanket at 12.6-cm (triangles) and 70-cm (crosses) wavelengths. Both histograms are normalized to an arbitrary vertical scale. Data at 70-cm wavelength are from *Campbell et al.* [2007].

example, Figure 4 shows a 14.8-km diameter crater, Rabbi Levi L, in the floor of the 82-km crater Rabbi Levi. Strong backscatter and high values of the CPR occur only in the interior of this crater, and nearby craters have similar streaks and patches along their inner walls. Even after spatially averaging over a large number of independent measurements, the circular polarization ratio along the northern and eastern crater interior walls has maximum values approaching 3

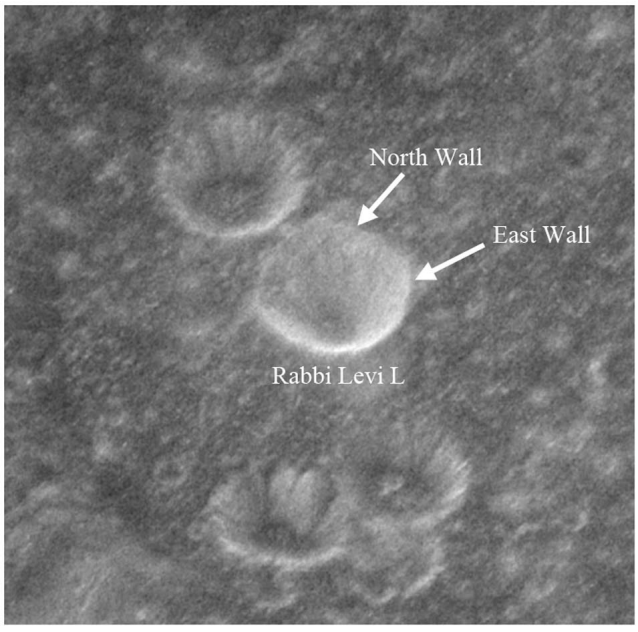

Figure 4. Same-sense circular polarization, 12.6-cm radar image of Rabbi Levi L crater (center location 34.75°S, 22.96°E), with arrows noting regions sampled for CPR distribution in Figure 5. Image size about 60 km by 60 km. North toward top. Radar illumination is from approximately the top of the image; radar incidence angle about 36°. Spatial resolution of the image is 80 m per pixel.

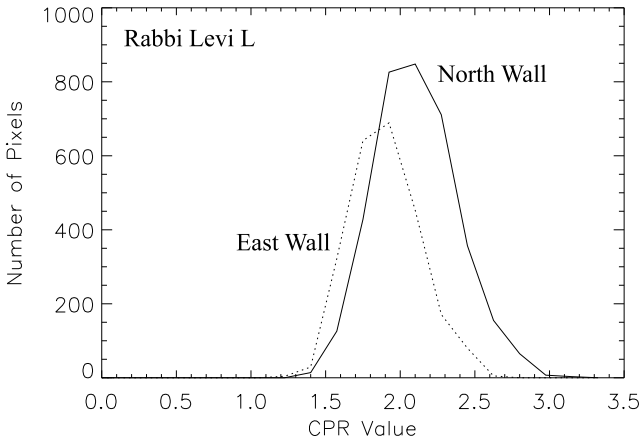

Figure 5. Histograms of 12.6-cm CPR values for sample sites along the northern and eastern interior walls of crater Rabbi Levi L. Echoes in the two circular polarization states were averaged over a total of 484 looks per sample to reduce speckle uncertainty.

(Figure 5). As expected, there is an increase in μ_c with local incidence angle, with the northern wall having the greatest tilt away from the incident beam and higher polarization ratios. There is little radar enhancement associated with the rim or proximal ejecta blanket of 10–15 km diameter craters in the floor of Rabbi Levi, suggesting that they are relatively old and most near-surface ejecta blocks have been broken down by micrometeorite bombardment. The high degree of radar echo and CPR enhancement from the interior must thus come from "shedding" of boulders or fragments of a competent layer near the top of the inner walls, perhaps associated with impact melt [*Campbell and Campbell*, 2006] linked with basin-derived plains units mapped in this area by *Scott* [1972].

[12] The dual-polarization Earth-based observations, and orbital MiniRF data, also allow calculation of a "degree of polarization" and "degree of linear polarization" from the four measured Stokes parameters:

$$\begin{vmatrix} S_1 \\ S_2 \\ S_3 \\ S_4 \end{vmatrix} = \begin{vmatrix} \langle A_L^2 \rangle + \langle A_R^2 \rangle \\ 2\langle A_L A_R \cos\delta \rangle \\ 2\langle A_L A_R \sin\delta \rangle \\ \langle A_L^2 \rangle - \langle A_R^2 \rangle \end{vmatrix} \tag{1}$$

where A_L and A_R are the voltages measured in the left- and right-circular polarized channels, δ is their relative phase, and $\langle\rangle$ denotes a time average. Any orthogonal polarization set [e.g., *Raney*, 2007] may also be used to form the Stokes vector terms. The degree of polarization is

$$DP = \frac{\left(S_2^2 + S_3^2 + S_4^2\right)^{1/2}}{S_1} \tag{2}$$

The degree of linear polarization is

$$DLP = \frac{\sqrt{S_2^2 + S_3^2}}{S_1} \tag{3}$$

where the total power in S_1 is typically corrected for any system noise component (which is canceled out by the cross-correlation that yields S_2 and S_3). A strong component of linear-polarized echo is typically associated with scattering from subsurface rocks or rough interfaces beneath smooth mantling material [*Carter et al.*, 2004, 2011]. Surface scattering, or a rough interface above a subsurface reflector, rapidly diminishes the correlation between the two polarization components. In this situation, the DLP is very low, and the DP is related to the circular polarization ratio:

$$DP \approx \frac{|S_4|}{S_1} = \left(\frac{|\mu_c - 1|}{\mu_c + 1}\right) \tag{4}$$

This has a maximum value of unity when μ_c is zero, declines to zero when $\mu_c = 1$, and rises again for larger values of the CPR. In the 12.6-cm Earth-based radar data for the Tycho floor and ejecta, the linear-polarized echo component is negligible, so the degree of polarization provides no additional information on possible scattering mechanisms.

3. Scattering Mechanisms Associated With High CPR

3.1. Scattering Matrix Representation

[13] An examination of the scattering matrix representation of radar echoes provides insight into how enhanced μ_c values arise. We begin with the definition of the SC and OC backscatter coefficients, σ^0_{ij}, from elements of the 2 × 2 scattering matrix, **S**, where S_{ij} describes the complex-valued voltage measured for transmit polarization *i* and receive polarization *j*. In the linear-polarized nomenclature for the scattering matrix terms these polarization states are either horizontal (H) or vertical (V). The 4 × 4 Stokes matrix [*van Zyl et al.*, 1987] contains the real-valued cross products of the scattering matrix elements, and relates the radar echo power to the polarization of the transmitted and received signals. The two circular polarization echoes are given by [*Campbell*, 2002]

$$\sigma^0_{SC} = \frac{1}{4}\left[S_{HH}S^*_{HH} + S_{VV}S^*_{VV} + 4S_{HV}S^*_{HV} + 4\mathrm{Im}\left(S_{VH}S^*_{VV} - S_{HV}S^*_{HH}\right) - 2\mathrm{Re}\left(S_{HH}S^*_{VV}\right)\right] \tag{5}$$

$$\sigma^0_{OC} = \frac{1}{4}\left[S_{HH}S^*_{HH} + S_{VV}S^*_{VV} + 2\mathrm{Re}\left(S_{HH}S^*_{VV}\right)\right] \tag{6}$$

where the asterisk denotes a complex conjugate. For natural surfaces, there is no evidence of significant correlation between the cross-polarized (HV, VH) and like-polarized (HH, VV) linear components, so we set that term of (5) to zero. Writing the appropriate cross products in terms of backscatter coefficients yields

$$\sigma^0_{SC} = \frac{1}{4}\left[\sigma^0_{HH} + \sigma^0_{VV} + 4\sigma^0_{HV} - 2\mathrm{Re}\left(S_{HH}S^*_{VV}\right)\right] \tag{7}$$

$$\sigma^0_{OC} = \frac{1}{4}\left[\sigma^0_{HH} + \sigma^0_{VV} + 2\mathrm{Re}\left(S_{HH}S^*_{VV}\right)\right] \tag{8}$$

This shows that μ_c depends upon the relative strengths of σ^0_{HV}, σ^0_{HH}, and σ^0_{VV}, and on the real part of the like-polarized correlation. We define the ratio of HH- to VV-polarized

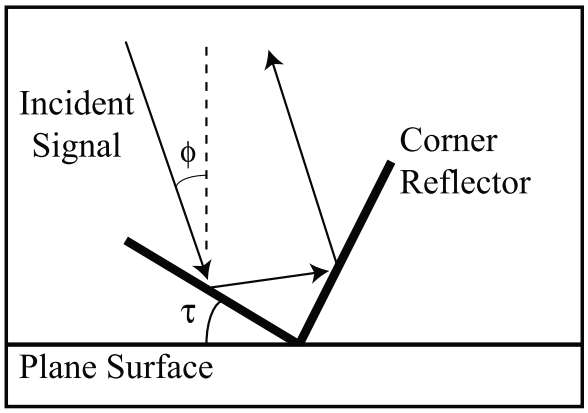

Figure 6. Diagram showing scattering geometry for a corner reflector. The vertical dashed line is the normal to the background plane surface.

backscattered power as α. The $Re(S_{HH}S_{VV}^*)$ term can be normalized to yield a ratio termed here β:

$$\beta = \frac{Re\left[S_{HH}S_{VV}^*\right]}{\sqrt{S_{HH}^2 S_{VV}^2}} = \frac{Re\left[S_{HH}S_{VV}^*\right]}{\sqrt{\sigma_{HH}^0 \sigma_{VV}^0}} \tag{9}$$

This parameter has a range from -1, corresponding to an ideal double-bounce return, to 1, corresponding to an ideal single-bounce reflection from radar-facing surface facets [*Boerner et al.*, 1987; *van Zyl*, 1989; *Freeman and Durden*, 1998; *Sato et al.*, 2005].

3.2. Dihedral Scattering

[14] A frequently cited physical model for generating high circular polarization ratios is termed dihedral scattering, where the radar signal is reflected back to the sensor via two mirror-like scattering events. The two-dimensional scattering geometry of pairs of facet-like surface elements that form a right angle can be described by a tilt angle, τ, the radar incidence angle with respect to a background plane surface, ϕ, and the real dielectric constant of the facets, ε_r (Figure 6). The applicable range of τ (in degrees) relative to the horizontal is from $-\phi$ to $(90 - \phi)$. Energy impinging on the first facet at local incidence angle $\phi_1 = (\phi + \tau)$ and reflecting back to the sensor after striking the second facet at incidence angle $\phi_2 = (90 - \phi_1)$ is modulated by the Fresnel reflection coefficients of the two events. The HH- and VV-polarized power reflection coefficients for the dihedral are

$$R_{HH} = R_H(\phi_1)R_H(\phi_2) = \frac{\sin^2(\theta_1 - \phi_1)}{\sin^2(\theta_1 + \phi_1)} \frac{\sin^2(\theta_2 - \phi_2)}{\sin^2(\theta_2 + \phi_2)} \tag{10}$$

$$R_{VV} = R_V(\phi_1)R_V(\phi_2) = \frac{\tan^2(\phi_1 - \theta_1)}{\tan^2(\theta_1 + \phi_1)} \frac{\tan^2(\phi_2 - \theta_2)}{\tan^2(\theta_2 + \phi_2)} \tag{11}$$

where the transmission angles are

$$\theta_1 = \sin^{-1}\left[\frac{\sin(\phi + \tau)}{\sqrt{\varepsilon_r}}\right] \tag{12}$$

$$\theta_2 = \sin^{-1}\left[\frac{\cos(\phi + \tau)}{\sqrt{\varepsilon_r}}\right] \tag{13}$$

There can be a strong difference in the relative magnitude of R_{HH} and R_{VV} for a dihedral feature, particularly where the incidence angle on one of the facets is close to the Brewster angle for that value of ε_r. We denote the ratio of HH- to VV-polarized backscattered power for a dihedral pair, or suite of such features, as α_D. For an ideal dihedral feature, σ_{HV}^0 is negligible, and β is -1. Under these conditions,

$$Re\left[S_{HH}S_{VV}^*\right] = -\sqrt{\sigma_{HH}^0 \sigma_{VV}^0} = -\sigma_{VV}^0 \sqrt{\alpha_D} \tag{14}$$

and the CPR can be simplified from equations (7) and (8):

$$\mu_c = \frac{\left(1 + \sqrt{\alpha_D}\right)^2}{\left(1 - \sqrt{\alpha_D}\right)^2} \tag{15}$$

Any single dihedral facet pair can have arbitrarily high values of μ_c, particularly where α_D is close to unity. To better represent a rugged surface, we must average the dihedral behavior shown by equations (10)–(11) over the range of possible geometries, and use the mean R_{HH} and R_{VV} values to define α_D for equation (15). This averaging assumes that every facet is of equal length, and weights the contributions of dihedrals by the projected scattering area ($\cos\phi_1 \cos\phi_2$) for a given geometry. The resulting average values of α_D and the CPR as a function of ε_r are shown in Figure 7. The value of α_D peaks at $\varepsilon_r \sim 6$, then declines toward unity for higher dielectric constants; the CPR in turn rises steadily. Average CPR values of 3–4 are associated with dielectric constants typical of dry geologic materials.

[15] The observed radar echo cannot arise solely from dihedral scattering features. The HH- and VV-polarized returns are a sum over all surface echoes, which must also include a component of single-bounce reflections ($\alpha = 1$, $\beta = 1$, $\mu_c = 0$) from favorably oriented facets. These single-scattering facets are "brighter" than any dihedral feature, since the double-bounce return is reduced by an additional factor of the Fresnel reflectivity. An increase in the real dielectric constant of one or both dihedral facets (i.e., bare

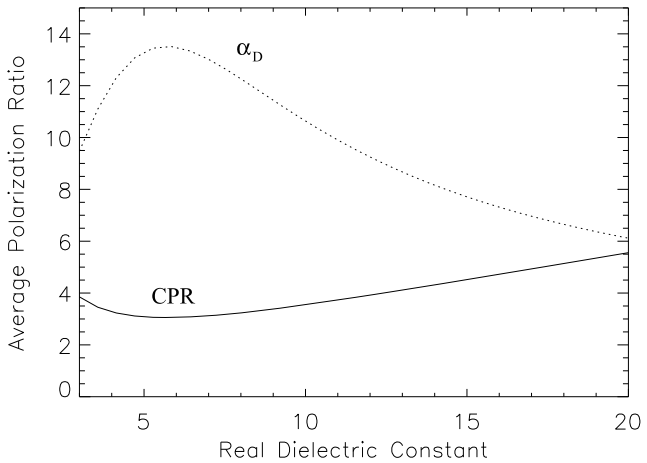

Figure 7. Circular polarization ratio (solid curve) and α_D, the ratio of HH-polarized to VV-polarized backscatter (dotted line), averaged over a distribution of randomly oriented dihedral facet pairs, as a function of the real dielectric constant of the facets.

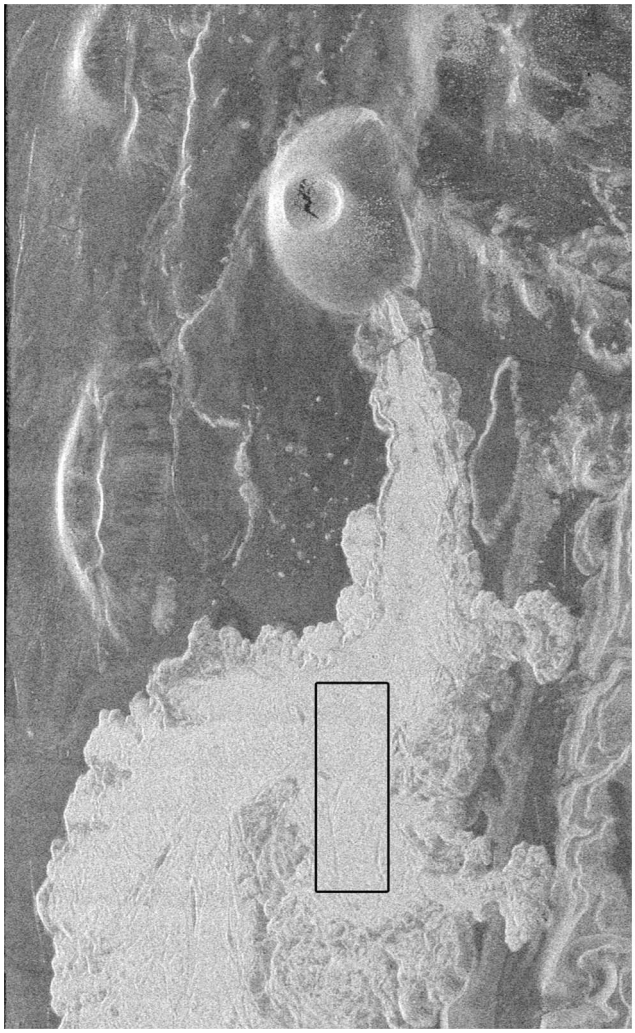

Figure 8. Radar image of SP cone and lava flow, Arizona (AIRSAR scene CM6453). Image height 6.9 km. Opposite-sense circular polarization; radar wavelength 24 cm. Radar illumination is from the left. The black box shows region used for analysis of echo statistics in Figure 9. The radar incidence angle for this sample region is about 34°.

rock versus regolith) enhances the relative contribution of double-bounce echoes to the overall return, as will coherent enhancement arising from reversed scattering paths [*Jin and Lax*, 1990]. In order to obtain CPR values of 2 to 3, however, the number of dihedral scattering paths within a radar resolution cell must still significantly exceed the population of single-scattering facets. This requirement is perhaps fulfilled only by surface roughness that yields a "sawtooth" structure, such as tilted plates, jointing, or closely spaced boulders preferentially larger than the illuminating wavelength.

[16] Diagnostic attributes of a dominantly dihedral scattering component include the high value of α and negative value of the like-polarized correlation term (and β). The latter behavior is sometimes noted in quad-pol decomposition models as a HH-VV phase term approaching 180° from vertical features like reeds or forest growth [*Ulaby et al.*, 1987; *Freeman and Durden*, 1998]. We also note that the CPR of randomly oriented dihedral features will rise with the surface dielectric constant, which could be important in radar studies of high-reflectivity regions on Venus [e.g., *Campbell et al.*, 1999].

3.3. Scattering From Dipole Elements

[17] The dihedral scattering model requires locally smooth facets, at least a few radar wavelengths in extent, which form backscattering right-angle pairs. Even allowing for the three-dimensional nature of a real surface, and the possibility that reflecting facets may be separated by some distance and still satisfy the double reflection geometry, dihedral features may be uncommon in geologic settings. A more ubiquitous type of scattering feature is ground cracks or rock edges that behave as dipole-like elements. Each such element has a signature dependent on its orientation with respect to the incident signal polarization. Taken as a collection of randomly oriented dipoles, a rough surface has these average backscatter properties:

$$\sigma^0_{HH} = \sigma^0_{VV} = 3\sigma^0_{HV} = \frac{3}{8}RP_0 \tag{16}$$

$$\beta = 1/3 \tag{17}$$

where P_0 is the illuminating power and R is a scaling factor that captures the effective gain or reflectivity of the individual dipoles [*Campbell et al.*, 1993; *Freeman and Durden*, 1998; *Campbell*, 2002]. Plugging these values into equations (7) and (8) shows that $\mu_c = 1$. The single-scattering model of randomly oriented dipoles appears to explain much of the depolarization in radar echoes from a range of surfaces [*Campbell et al.*, 1993; *Freeman and Durden*, 1998; *Plaut et al.*, 2004; *Campbell*, 2009], but does not produce the maximum degree of enhancement observed in rugged lunar settings.

[18] If the energy scattered by a collection of random dipoles is intercepted and scattered a second time by a dipole-like feature, the net backscatter is

$$\begin{aligned}\sigma^D_{HH} &= \left(\frac{3R}{8}\right)\sigma^S_{HH} + \left(\frac{R}{8}\right)\sigma^S_{HV} \\ &= \left(\frac{3R}{8}\right)\left(\frac{3RP_o}{8}\right) + \left(\frac{R}{8}\right)\left(\frac{RP_o}{8}\right) = \frac{5R^2P_o}{32}\end{aligned} \tag{18}$$

$$\begin{aligned}\sigma^D_{HV} &= \left(\frac{R}{8}\right)\sigma^S_{HH} + \left(\frac{3R}{8}\right)\sigma^S_{HV} \\ &= \left(\frac{R}{8}\right)\left(\frac{3RP_o}{8}\right) + \left(\frac{3R}{8}\right)\left(\frac{RP_o}{8}\right) = \frac{3R^2P_o}{32}\end{aligned} \tag{19}$$

where the D and S superscripts refer to the echoes from the double-bounce and single-bounce events. We see that the double-bounce scenario leads to a substantially higher degree of depolarization ($\sigma^0_{HV}/\sigma^0_{HH}$ = 3/5) for a linear-polarized illuminating signal. Another diagnostic aspect is that β declines from the 1/3 value of the single-scattering dipole case, and for a cloud distribution will approach zero [*Oh et al.*, 2002; *Mattia et al.*, 1997]. The $\sigma^0_{HH}/\sigma^0_{VV}$ ratio, α, is again near unity.

[19] While a double-bounce event between dipole-like rock edges will be perhaps 10% the strength of a single-

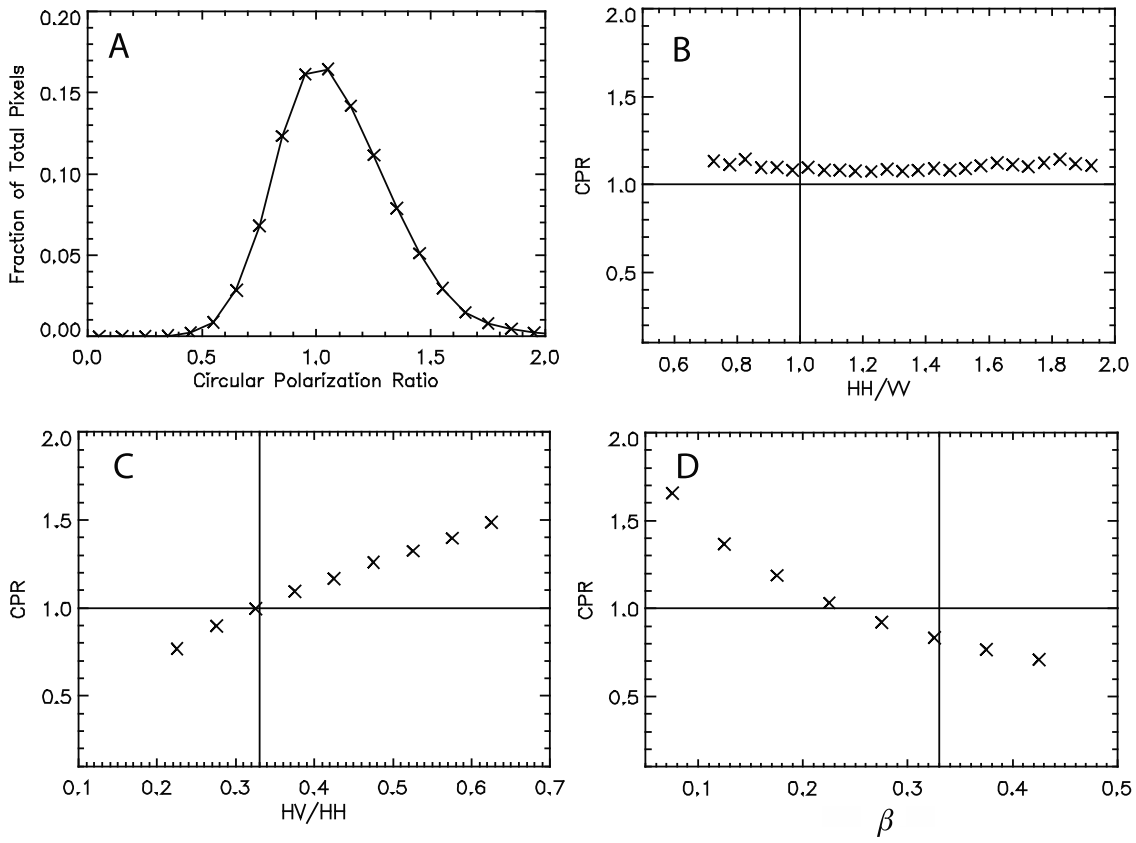

Figure 9. (a) Histogram of circular polarization ratio (CPR) values at 24-cm wavelength for sample area of SP flow noted on Figure 8. (b) Average value of the CPR for the sample region as a function of the ratio between the HH- and VV-polarized echoes. (c) Average value of the CPR as a function of the ratio between HV- and HH-polarized echoes. (d) Average value of the CPR for the sample region as a function of the normalized HH-VV correlation, β. Solid lines in Figures 9b–9d denote the behaviors expected for single-scattering, randomly oriented dipoles.

bounce event (given typical rock reflectivity of 0.1), there are potentially far more opportunities for this type of scattering to occur in rugged terrain. Dipole-like elements are effective scatterers in any position on the surface. The issue is simply visibility – how often can energy scattered by an initial dipole element encounter another such feature and return to the sensor? The ideal situation is a cloud-like distribution in space, where almost every dipole can intercept energy from every other. The other end-member is cracks in a horizontal planar surface, which reflect on the first bounce but allow few multiple-scattering events. Rugged surfaces progressively allow more double-bounce interactions as the vertical scale of the roughness increases. Setting $\alpha = 1$, the ratio of equations (7) to (8) is

$$\mu_c = \left(1 + 2\frac{\sigma^0_{HV}}{\sigma^0_{HH}} - \beta\right)/(1+\beta) \qquad (20)$$

When double-bounce scattering among dipole-like elements is strong, then β approaches zero and $\sigma^0_{HV}/\sigma^0_{HH} = 3/5$ from equations (18)–(19), so μ_c has a maximum possible value of 2.2. In neither dipole model does the dielectric constant of the surface impact the upper bound on the circular polarization ratio, but enhanced surface reflectivity will increase the relative importance of any double-bounce component.

4. High CPR Values From SP Flow

[20] SP Flow in northern Arizona is a geologic surface that might allow efficient multiple scattering of a radar signal due to abundant decimeter-scale, smooth-sided boulders [*Schaber et al.*, 1980; *Campbell et al.*, 1993]. We utilized 24-cm wavelength radar data collected by the quad-pol NASA/JPL AIRSAR instrument. The study area is shown in Figure 8, and we averaged the original 4-look pixels with a 5 × 5 boxcar filter to yield ratio values with about 10% uncertainties. A histogram of CPR values over the sample area shows that μ_c is often >1 but is limited to less than ~2 (Figure 9a).

[21] We can use the correlations between radar polarization ratios to infer the dominant scattering mechanism for this rugged surface. First, there is no correlation between μ_c and the $\sigma^0_{HH}/\sigma^0_{VV}$ ratio (Figure 9b); such correlation is a key attribute of dihedral scattering (15). Second, there is a strong positive correlation between μ_c and the $\sigma^0_{HV}/\sigma^0_{HH}$ ratio (Figure 9c), which is expected for both the single- and double-bounce dipole models. Finally, we note the negative correlation between μ_c and β (Figure 9d), consistent with a

decline in coherence between the HH- and VV-polarized returns with increasing amounts of either dipole-scattering mechanism relative to any facet-like echo component.

[22] These behaviors, the upper limit of about 0.5 on $\sigma^0_{HV}/\sigma^0_{HH}$, and the lower limit of about 0.05 on β, are all consistent with the double-bounce dipole model for creating the highest CPR enhancements from SP Flow. It should be noted that the average behavior over the entire study area is $\mu_c \sim 1$ and $\sigma^0_{HV}/\sigma^0_{HH} \sim 1/3$, so in many parts of the flow the single-scattering, dipole-like model predominates. Strong dihedral scattering may be responsible for pixels with high $\sigma^0_{HH}/\sigma^0_{VV}$ ratios, but this mechanism does not cause elevated CPR values (Figure 9b) as it does in urban settings [e.g., *van Zyl*, 1989].

5. Discussion and Conclusions

[23] Any surface of moderate or greater roughness will exhibit backscatter components from all of the mechanisms discussed (facets, dihedrals, and dipoles). Each of these mechanisms may also arise in scattering from objects or interfaces in and beneath a planetary regolith, with their contributions to the total observed echo diminished by attenuation in the material and the reduced dielectric contrast between rocks and soil (relative to rocks and vacuum). Efforts to decompose radar echoes into physically meaningful components using their polarization properties typically exploit the full range of information contained in the quad-pol format [e.g., *Freeman and Durden*, 1998]. The dual-pol measurements used in planetary studies are more limited in their degrees of freedom, and for many rough surfaces the correlation measured by the Stokes-vector S_2 and S_3 terms (1) may be negligible. The analysis of SP Flow shows how important the fully polarimetric data are to understanding the dominant scattering mechanisms and associated geologic properties.

[24] The circular polarization ratio does provide significant information on the physical characteristics of the target surface. Given the upper limits of the dipole scattering model, we may infer that the highest μ_c values of 2.5 to 3 for Tycho and other rough sites on the Moon are caused by dihedral scattering between nearby rocks or between rock faces and the soil surface. Achieving these high values requires that double-bounce backscattering paths within a target area be significantly more numerous than single-bounce geometries, implying non-random roughness structures and scales. At SP Flow, high-CPR areas are more consistent with multiple scattering among rock edges or cracks. The lack of obvious dihedral signatures at SP, when they appear so necessary to explain the high μ_c values for Tycho, may be due to a difference in the scales of roughness. There are abundant smooth rock faces across the surface of SP flow, but these are typically a few decimeters in extent. The floor of Tycho is populated by boulders and blocks 3–10 m in diameter (Figure 2), and thus provides the necessary smooth patches for effective dihedral structures.

[25] The Maxwell Montes on Venus also display high μ_c, with maximum values at 12.6-cm wavelength of about 1.5 [*Campbell et al.*, 1999]. This same study found that the linear polarization ratio, analogous to $\sigma^0_{HV}/\sigma^0_{HH}$, has a maximum of about 0.5. As with other regions of Venus above about 6053-km planetary radius, Maxwell Montes has enhanced surface reflectivity, consistent with a real dielectric constant of 20 or more and a potentially very high imaginary component [e.g., *Simpson et al.*, 2009]. From Section 3, we expect that echoes arising from the dihedral mechanism will exhibit a steady increase in CPR as the real dielectric constant rises. While μ_c for Maxwell Montes does rise with surface reflectivity, values measured to date at few-km spatial resolution do not exceed 2, and the $\sigma^0_{HV}/\sigma^0_{HH}$ ratio approaches the 0.6 limit noted in equations (18)–(19). A combination of single and multiple scattering from randomly oriented dipoles is thus at least adequate to explain the current Maxwell observations.

[26] The dominance in these rough settings of scattering behavior similar to that of randomly oriented dipoles also suggests that this is a common "background" component in the lunar CPR signature. In areas where the loss tangent of the regolith is relatively low, such as highland material or low-ilmenite mare basalt, both single scattering and some degree of multiple scattering could occur from/between wavelength-scale rocks suspended in the soil [*Thompson et al.*, 1970]. This would enhance the CPR above that expected from surface scattering by individual rocks. *Campbell et al.* [2010] observe a rise in 12.6-cm wavelength μ_c for the lunar maria with lower ilmenite content, consistent with an increasing role for these subsurface echoes as the regolith becomes more radar-transparent. The same mechanism may occur in scattering from regolith on asteroids.

[27] In orbital radar studies of Mars, as with Earth-based radar studies of Mercury [*Harmon et al.*, 2011], detection and mapping of clean ice in shallow, dust-covered patches [e.g., *Byrne et al.*, 2009] will exploit the distinctive polarization properties of the coherent backscatter mechanism [*Black et al.*, 2001]. The enhanced CPR and strong echoes of slab-like ice will be readily distinguishable from the average properties of a lunar-like regolith [*Campbell et al.*, 2010]. Ambiguities arise mainly where the ice is at low volume fractions [*Thompson et al.*, 2011; *Fa et al.*, 2011] or the terrain of interest is on the rugged walls or proximal ejecta of impact craters. In contrast, most northern plains regions of Mars have CPR values [*Harmon and Nolan*, 2007] well below the maximum of 0.6 found for "typical" rough surfaces [*Campbell*, 2009]. This study suggests that fully polarimetric radar can provide stronger constraints on the dominant scattering regime, and thus focus work on regions with signatures most consistent with subsurface ice. Previous work shows that longer wavelength radar echoes exhibit lower μ_c for any given surface roughness or population of suspended rocks [*Campbell*, 2009], and greater penetration depth in mantling materials [*Campbell et al.*, 2004], so moving toward lower frequencies (L- or P-band in contrast to X-band or S-band) will further reduce ambiguities in the search for Martian ice deposits.

[28] **Acknowledgments.** The author thanks C. Neish and W. Fa for helpful reviews of the paper and M. Shepard for comments on earlier drafts. This work was supported in part by grants from the NASA Planetary Astronomy and Planetary Geology and Geophysics Programs.

References

Benner, L. A. M., et al. (2008), Near-Earth asteroid surface roughness depends on compositional class, *Icarus*, *198*, 294–304, doi:10.1016/j.icarus.2008.06.010.

Black, G. J., D. B. Campbell, and P. D. Nicholson (2001), Icy Galilean satellites: Modeling radar reflectivities as a coherent backscatter effect, *Icarus*, *151*, 167–180, doi:10.1006/icar.2001.6616.

Black, G. J., D. B. Campbell, and L. M. Carter (2011), Ground-based radar observations of Titan: 2000–2008, *Icarus*, *212*, 300–320, doi:10.1016/j.icarus.2010.10.025.

Boerner, W., B. Foo, and H. J. Eom (1987), Interpretation of the polarimetric co-polarization phase term in radar images obtained with the JPL airborne L-band SAR system, *IEEE Trans. Geosci. Remote Sens.*, *GE-25*, 77–82, doi:10.1109/TGRS.1987.289783.

Byrne, S., et al. (2009), Distribution of mid-latitude ground ice on Mars from new impact craters, *Science*, *325*, 1674–1676, doi:10.1126/science.1175307.

Campbell, B. A. (2002), *Radar Remote Sensing of Planetary Surfaces*, Cambridge Univ. Press, Cambridge, U. K.

Campbell, B. A. (2009), Scale-dependent surface roughness behavior and its impact on empirical models for radar backscatter, *IEEE Trans. Geosci. Remote Sens.*, *47*, 3480–3488, doi:10.1109/TGRS.2009.2022752.

Campbell, B. A., and D. B. Campbell (2006), Surface properties in the south polar region of the Moon from 70-cm radar polarimetry, *Icarus*, *180*, 1–7, doi:10.1016/j.icarus.2005.08.018.

Campbell, B. A., S. H. Zisk, and P. J. Mouginis-Mark (1989), A quad-pol radar scattering model for use in remote sensing of lava flow morphology, *Remote Sens. Environ.*, *30*, 227–237, doi:10.1016/0034-4257(89)90064-3.

Campbell, B. A., R. E. Arvidson, and M. K. Shepard (1993), Radar polarization properties of volcanic and playa surfaces: Applications to terrestrial remote sensing and Magellan data interpretation, *J. Geophys. Res.*, *98*, 17,099–17,113, doi:10.1029/93JE01541.

Campbell, B. A., D. B. Campbell, and C. DeVries (1999), Surface processes in the Venus highlands: Results from analysis of Magellan and Arecibo data, *J. Geophys. Res.*, *104*, 1897–1916, doi:10.1029/1998JE900022.

Campbell, B. A., T. Maxwell, and A. Freeman (2004), Mars orbital SAR: Obtaining geologic information from radar polarimetry, *J. Geophys. Res.*, *109*, E07008, doi:10.1029/2004JE002264.

Campbell, B. A., D. B. Campbell, J. L. Margot, R. R. Ghent, M. Nolan, J. Chandler, L. M. Carter, and N. J. S. Stacy (2007), Focused 70-cm radar mapping of the Moon, *IEEE Trans. Geosci. Remote Sens.*, *45*(12), 4032–4042, doi:10.1109/TGRS.2007.906582.

Campbell, B. A., B. R. Hawke, and D. B. Campbell (2009), Surface morphology of domes in the Marius Hills and Mons Rumker regions of the Moon from Earth-based radar data, *J. Geophys. Res.*, *114*, E01001, doi:10.1029/2008JE003253.

Campbell, B. A., L. M. Carter, D. B. Campbell, M. Nolan, J. Chandler, R. R. Ghent, B. R. Hawke, R. F. Anderson, and K. Wells (2010), Earth-based S-band radar mapping of the Moon: New views of impact melt distribution and mare physical properties, *Icarus*, *208*, 565–573, doi:10.1016/j.icarus.2010.03.011.

Campbell, D. B., J. F. Chandler, S. J. Ostro, G. H. Pettengill, and I. I. Shapiro (1978), Galilean satellites: 1976 radar results, *Icarus*, *34*, 254–267, doi:10.1016/0019-1035(78)90166-5.

Campbell, D. B., B. A. Campbell, L. M. Carter, J. L. Margot, and N. J. S. Stacy (2006), Lunar polar ice: No evidence for thick deposits at the south pole, *Nature*, *443*, 835–837, doi:10.1038/nature05167.

Carter, L. M., D. B. Campbell, and B. A. Campbell (2004), Impact crater related surficial deposits on Venus: Multi-polarization radar observations with Arecibo, *J. Geophys. Res.*, *109*, E06009, doi:10.1029/2003JE002227.

Carter, L. M., D. B. Campbell, and B. A. Campbell (2011), Geologic studies of planetary surfaces using radar polarimetric imaging, *Proc. IEEE*, *99*, 770–782, doi:10.1109/JPROC.2010.2099090.

Fa, W., M. A. Wieczorek, and E. Heggy (2011), Modeling polarimetric radar scattering from the lunar surface: Study on the effect of physical properties of the regolith layer, *J. Geophys. Res.*, *116*, E03005, doi:10.1029/2010JE003649.

Freeman, A., and S. L. Durden (1998), A three-component scattering model for polarimetric SAR data, *IEEE Trans. Geosci. Remote Sens.*, *36*, 963–973, doi:10.1109/36.673687.

Harmon, J. K., and M. Nolan (2007), Arecibo radar imaging of Mars during the 2005 opposition, *Seventh International Conference on Mars, July 9–13, 2007, Pasadena CA* [CD-ROM], LPI Contrib., *1353*, Abstract 3136.

Harmon, J. K., et al. (1994), Radar mapping of Mercury's polar anomalies, *Nature*, *369*, 213–215, doi:10.1038/369213a0.

Harmon, J. K., R. E. Arvidson, E. A. Guinness, B. A. Campbell, and M. A. Slade (1999), Mars mapping with delay-Doppler radar, *J. Geophys. Res.*, *104*, 14,065–14,089, doi:10.1029/1998JE900042.

Harmon, J. K., P. J. Perillat, and M. A. Slade (2001), High-resolution radar imaging of Mercury's north pole, *Icarus*, *149*, 1–15, doi:10.1006/icar.2000.6544.

Harmon, J. K., M. A. Slade, and M. S. Rice (2011), Radar imagery of Mercury's putative polar ice: 1999–2005 Arecibo results, *Icarus*, *211*, 37–50, doi:10.1016/j.icarus.2010.08.007.

Hiesinger, H., C. H. van der Bogert, M. S. Robinson, K. Klemm, and D. Reiss, and the LRO Team (2010), New crater size-frequency distribution measurements for Tycho Crater based on Lunar Reconnaissance Orbiter Camera images, *Lunar Planet. Sci. XLI*, Abstract 2287.

Jin, Y., and M. Lax (1990), Backscattering enhancement from a randomly rough surface, *Phys. Rev. B*, *42*, 9819–9829, doi:10.1103/PhysRevB.42.9819.

Mattia, F., T. Le Toan, J.-C. Souyris, G. De Carolis, N. Floury, F. Posa, and G. Pasquariello (1997), The effect of surface roughness on multifrequency polarimetric SAR data, *IEEE Trans. Geosci. Remote Sens.*, *35*, 954–966, doi:10.1109/36.602537.

Oh, Y., K. Sarabandi, and F. T. Ulaby (2002), Semi-empirical model of the ensemble-averaged differential Mueller matrix for microwave backscattering from bare soil surfaces, *IEEE Trans. Geosci. Remote Sens.*, *40*, 1348–1355, doi:10.1109/TGRS.2002.800232.

Ostro, S. J., et al. (1992), Europa, Ganymede, and Callisto: New radar results from Arecibo and Goldstone, *J. Geophys. Res.*, *97*, 18,227–18,244, doi:10.1029/92JE01992.

Plaut, J. J., S. W. Anderson, D. A. Crown, E. R. Stofan, and J. J. van Zyl (2004), The unique radar properties of silicic lava domes, *J. Geophys. Res.*, *109*, E03001, doi:10.1029/2002JE002017.

Raney, R. K. (2007), Hybrid-polarity SAR architecture, *IEEE Trans. Geosci. Remote Sens.*, *45*, 3397–3404, doi:10.1109/TGRS.2007.895883.

Rignot, E. (1995), Backscatter model for the unusual radar properties of the Greenland ice sheet, *J. Geophys. Res.*, *100*, 9389–9400, doi:10.1029/95JE00485.

Robinson, M. S., et al. (2010), Lunar Reconnaissance Orbiter Camera (LROC) instrument overview, *Space Sci. Rev.*, *150*, 81–124, doi:10.1007/s11214-010-9634-2.

Sato, R., K. Hayashi, Y. Yamaguchi, and H. Yamada (2005), Polarimetric scattering by a finite dihedral corner reflector, paper presented at ISAP2005, Inst. of Electr. and Electr. Eng., Seoul, Korea.

Schaber, G. G., C. Elachi, and T. G. Farr (1980), Remote sensing of SP mountain and SP lava flow in North-central Arizona, *Remote Sens. Environ.*, *9*, 149–170, doi:10.1016/0034-4257(80)90005-X.

Scott, D. H. (1972), Geologic map of the Maurolycus quadrangle of the Moon, *U.S. Geol. Surv. Misc. Invest. Map I-695*.

Shepard, M. K., K. M. Kressler, B. E. Clark, M. E. Ockert-Bell, M. C. Nolan, E. S. Howell, C. Magri, J. D. Giorgini, L. A. M. Benner, and S. J. Ostro (2008), Radar observations of E-class asteroids 44 Nysa and 434 Hungaria, *Icarus*, *195*, 220–225, doi:10.1016/j.icarus.2007.12.018.

Simpson, R. A., G. L. Tyler, B. Hausler, R. Mattei, and M. Patzold (2009), Venus Express bistatic radar: High-elevation anomalous reflectivity, *J. Geophys. Res.*, *114*, E00B41, doi:10.1029/2008JE003156.

Smith, P. H., et al. (2009), H_2O at the Phoenix landing site, *Science*, *325*, 58–61, doi:10.126/science.1172339.

Spudis, P. D., et al. (2010), Initial results for the north pole of the Moon from Mini-SAR, Chandrayaan-1 mission, *Geophys. Res. Lett.*, *37*, L06204, doi:10.1029/2009GL042259.

Thompson, T. W., J. B. Pollack, M. J. Campbell, and B. T. O'Leary (1970), Radar maps of the Moon at 70-cm wavelength and their interpretation, *Radio Sci.*, *5*, 253–262, doi:10.1029/RS005i002p00253.

Thompson, T. W., E. A. Ustinov, and E. Heggy (2011), Modeling radar scattering from icy lunar regoliths at 13 cm and 4 cm wavelengths, *J. Geophys. Res.*, *116*, E01006, doi:10.1029/2009JE003368.

Ulaby, F. T., D. Held, M. C. Dobson, K. C. McDonald, and T. B. Senior (1987), Relating polarization phase difference of SAR signals to scene properties, *IEEE Trans. Geosci. Remote Sens.*, *GE-25*, 83–92, doi:10.1109/TGRS.1987.289784.

van Zyl, J. J. (1989), Unsupervised classification of scattering behavior using radar polarimetry data, *IEEE Trans. Geosci. Remote Sens.*, *27*, 36–45, doi:10.1109/36.20273.

van Zyl, J. J., H. A. Zebker, and C. Elachi (1987), Imaging radar polarization signatures: Theory and observations, *Radio Sci.*, *22*, 529–543, doi:10.1029/RS022i004p00529.